Temperature drift rate for nuclear terms of the NV-center ground-state Hamiltonian

Vladimir V. Soshenko,[1] Vadim V. Vorobyov,[1,6] Stepan V. Bolshedvorskii,[1,2] Olga Rubinas,[2] Ivan Cojocaru,[1,3]
Boris Kudlatsky,[2,3] Anton I. Zeleneev,[2,3] Vadim N. Sorokin,[1,3] Andrey N. Smolyaninov,[4] and Alexey V. Akimov [1,3,5]

[1]*P. N. Lebedev Physical Institute, 53 Leninskij Prospekt, Moscow, 119991, Russia*
[2]*Moscow Institute of Physics and Technology, 9 Institutskiy per., Dolgoprudny, Moscow Region, 141700, Russia*
[3]*Russian Quantum Center, 100 Novaya St., Skolkovo, Moscow, 143025, Russia*
[4]*Photonic Nano-Meta Technologies, The Territory of Skolkovo Innovation Center, Str. Nobel b.7, Moscow, 143026, Russia*
[5]*Texas A&M University, 4242 TAMU, College Station, Texas 77843, USA*
[6]*3rd Institut of Physics, IQST and Centre for Applied Quantum Technologies, University of Stuttgart,*
Pfaffenwaldring 57, 70569 Stuttgart, Germany

The nitrogen-vacancy (NV) center in diamond has been found to be a powerful tool for various sensing applications. In particular, in ensemble-based sensors, the main "workhorse" so far has been optically detected electron resonance. Utilization of the nuclear spin has the potential to significantly improve sensitivity in rotation and magnetic field sensors. Ensemble-based sensors consume a substantial amount of power, leading to noticeable heating of the diamond and thus requiring an understanding of temperature-related shifts. In this paper, we provide a detailed study of the temperature shift of the hyperfine components of the NV center.

I. INTRODUCTION

The use of nitrogen-vacancy (NV) color centers in diamond has a number of important applications in bioimaging, sensing, and biosensing [1–6]. It also allows long-lasting (more than 1 s) room-temperature, quantum memory [7]. Nuclear spin plays an important role in many of these applications. As an example, the long-lasting quantum memory utilizes nuclear spin (since it could be robust against spin-bath noise) and is very weakly modified in optical transitions [8,9]. The storage properties of nuclear spin enhance sensor sensitivity [10], and nuclear spin could be used as a direct sensing element, for example, for rotation sensing [11,12]. Its applications range from enhancing magnetic resonance imaging sensitivity in nanodiamond-based, biocompatible sensors via dynamical nuclear polarization [3,13,14] to nonvolatile quantum memory [15] or room-temperature quantum registers [7,8,16]. While the most impressive experimental results were achieved with ^{13}C nuclear spin in isotopically pure diamond, nitrogen-related spin also has great potential for ensemble-based measurements since it has a definite location within the NV color center. In particular, rotation sensors benefit from this advantage [11,12].

Sensing applications require a deep understanding of the systematic shift of spin-related energy levels. In particular, applications directly involving a narrow (kilohertz-range) nuclear spin-flipping transitions within one electronic state are very sensitive to the exact splitting of the hyperfine structure. This is important in both estimating the systematics of measurement output and the stable operation of sensor-constituting blocks, e.g., for spin initialization, manipulation, and readout [9,11,12,17]. Practical ensemble-based sensors

typically use high optical pumping powers [18,19] to obtain a high signal-to-noise ratio, leading to considerable heating of the diamond. Thus, if not compensated for, temperature shifts may cause failure of the spin manipulation and a reduction in the overall sensor stability. While the diamond temperature could be monitored with the same NV center [20–22] using the temperature dependence of the optically detected magnetic resonance (ODMR) [20,23,24], feedback on the nuclear spin resonance requires an understanding of the temperature dependence of the hyperfine interaction.

In this paper, we experimentally investigate a temperature shift of nitrogen (^{14}N)-related spin transitions in the NV color center in diamond in the range from 305 to 350 K.

Measurement of the nuclear spin sensitivity to temperature was performed via the detection of ODMR in an ensemble of NV centers [2,25–27] [see Fig. 1(a) and Appendix A]. In the presence of nitrogen nuclear spin, ODMR with a defined electron-spin component $m_s = 0, \pm 1$ splits into three components [Fig. 1(b)]. The splitting is nevertheless different in the ground $m_s = 0$ and excited $m_s = -1$ states. This difference in splitting allows one to address nuclear sublevels independently in either the excited or ground state. Thus, if ODMR is observed at the microwave (MW) field frequency, corresponding to the particular hyperfine component, the strength of the resonance may be modified if transitions between hyperfine components are induced by the radio frequency (rf) field. The maximum effect of the rf field on ODMR transitions occurs when the rf field is exactly at resonance with rf transitions, thus allowing measurement of the rf transition frequency by the effect of the rf on ODMR [28].

To detect the positions of the nuclear and electron resonances, we applied a pulsed sequence, illustrated in Fig. 1(c).

(a) Diode laser

(b)

(c)
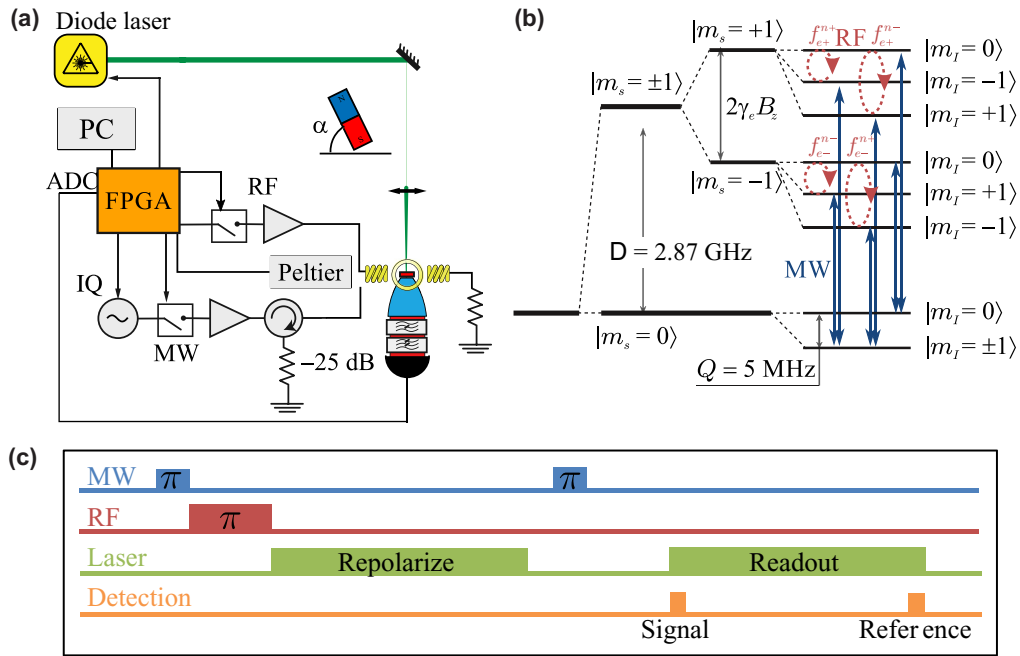
FIG. 1. (a) Experimental setup for nuclear spin spectroscopy of the NV-center ensemble. A FPGA was used to control the pulse sequence. (b) Energy levels of the ground state of an NV center. D stands for the zero-field splitting; Q, the hyperfine structure constant for splitting due to ^{14}N nuclear spin; and $2\gamma_{es}B$, Zeeman splitting between electron spins. The blue solid arrows show the allowed dipole MW transitions to the $m_s = \pm 1$ manifold, and the red circular dashed lines are allowed rf transitions of the nuclear spin in the $m_s = \pm 1$ manifold. (c) Pulse sequence of the experiment.

The main cycle of the sequence is similar to the nuclear recursive polarization sequence [9,17,28]. The NV center was first optically polarized with a green optical laser in an $m_s = 0$ manifold in the ground state and then transferred into an $m_s = \pm 1$ manifold using the selective MW π pulse [see Fig. 1(c)]. Then, the selective rf pulse was applied (see Appendix B), which, if resonant, mixes hyperfine levels of the selected magnetic manifold. The rf pulse was followed by an optical pulse that returned most of the population to the $m_s = 0$ manifold. This resulted in the hyperpolarization of ^{14}N nuclear spin. Another selective microwave π-pulse and optical detection resulted in the observation of the nuclear spin population at a state corresponding to the MW pulse frequency. Thus, when the rf field was resonant with the nuclear spin transition, the contrast was suppressed, indicating that the population was transferred out of that state.

To scan all nuclear transitions in the $m_s = \pm 1$ manifolds, the MW frequency was scanned within two bands near frequencies of 2837 and 2902 MHz, and the rf was swept in two bands near 2.8 and 7.1 MHz. To allow nuclear populations to thermalize, the MW frequency scan loop was nested in the rf scan loop (for more details, see Appendix C). The fluorescence of the NV center, detected in all four combinations of MW frequencies and rfs, is depicted in Fig. 2(a).

The electron transition frequencies were found by fitting the fluorescence spectrum along the MW axis with the sum of three Lorentzian curves [Fig 2(c)]. For this purpose, each spectrum was averaged over 100 realizations of fluorescence spectra along the MW frequency axis taken at an rf far from the nuclear transition frequency ($>$15-kHz detuning). Once the positions of the resonances in the MW spectra were

determined, the spectra obtained at all other rfs were fitted with only amplitudes of the resonances being free parameters. Thus, the hyperfine peak amplitude was determined. Figure 2(c) illustrates the amplitude of the peak, corresponding to $m_i = 0$ against the rf (for details, see Appendix D). The resulting curve, representing hyperfine transition resonance, was fitted with a single Lorentzian curve, the center of which was used as the position of the nuclear resonance for a given temperature.

To understand the contributions to the temperature-dependent shift of the observed nuclear resonance from different types of interactions, we consider the optical ground-state interaction Hamiltonian H for the nuclear spin in the NV center [29]:

$$H = h\left(QI_z^2 + S_z A_{\parallel} I_z + \gamma_n B_z I_z\right). \tag{1}$$

Here, Q is quadrupolar zero-field splitting for nuclear spin, I_z is nuclear spin projection on the z axis, S_z is electron spin projection on the z axis, $A_{\parallel}$ is longitudinal tensor component of the electron-nucleus spin-spin interaction, γ_n is nuclear spin gyromagnetic ratio, and B_z is external magnetic field. Here, we excluded off-diagonal terms in the Hamiltonian and calculated the second-order corrections separately (see Appendix E). Since the electronic spin in the ground state is 0, the nuclear state splitting in the ground state is independent of $A_{\parallel}$. By contrast, in the excited state, both $A_{\parallel}$ and Q contribute to the transition. For magnetic sublevels, $m_s = -1, +1$ allowed nuclear transitions from $m_i = 0$ ($\Delta m_i = \pm 1$) are at the frequencies $f_{e-}^{n\pm} = |Q \pm \gamma_n B_z \mp A_{\parallel}|$ and $f_{e+}^{n\pm} = |Q \pm \gamma_n B_z \pm A_{\parallel}|$ [Fig. 3(a)]. Here, the upper index describes the magnetic manifold, and the lower index $\pm$ corresponds
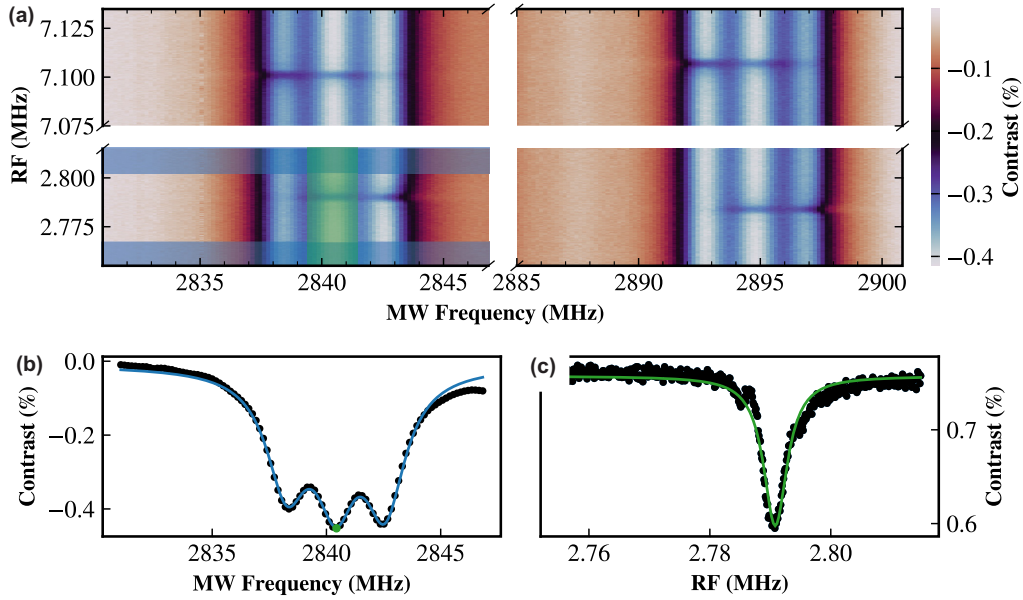
FIG. 2. (a) Two-dimensional (2D) scan of the rf and MW resonances. The light-blue rectangles show the data slice for panel (b), and the green rectangle shows the area discussed in (b) and (c). (b) Average of the cross sections in the 2D plot in panel (a), corresponding to the MW resonances not affected by the rf. The solid line corresponds to the fit with three Lorentzian curves. (c) Hyperfine component amplitude vs RF. The microwave frequency for this plot was fixed at the value indicated by the green dot in (b) (see text for more details). The solid line corresponds to the Lorentzian fit.

to nuclear transitions $|m_i = 0\rangle \rightarrow |m_i = \pm 1\rangle$. Knowing that $Q < A_\parallel < 0$ [29] for low B_z, we can expand the equations for $f_{e-}^{n\pm}$, $f_{e+}^{n\pm}$ t:

$$f_{e-}^{n\pm} = |Q| \mp |A_\parallel| \mp \gamma_n B_z \quad f_{e+}^{n\pm} = |Q| \pm |A_\parallel| \mp \gamma_n B_z. \quad (2)$$

To deduce Q, $A_\parallel$ from the rf resonance positions and neglect the Zeeman term, we use the following equations:

$$Q = -\frac{f_{e-}^{n-} + f_{e-}^{n+} + f_{e+}^{n-} + f_{e+}^{n+}}{4} \quad (3)$$

$$A_\parallel = -\frac{(f_{e-}^{n-} - f_{e-}^{n+}) - (f_{e+}^{n-} - f_{e+}^{n+})}{4} \quad (4)$$
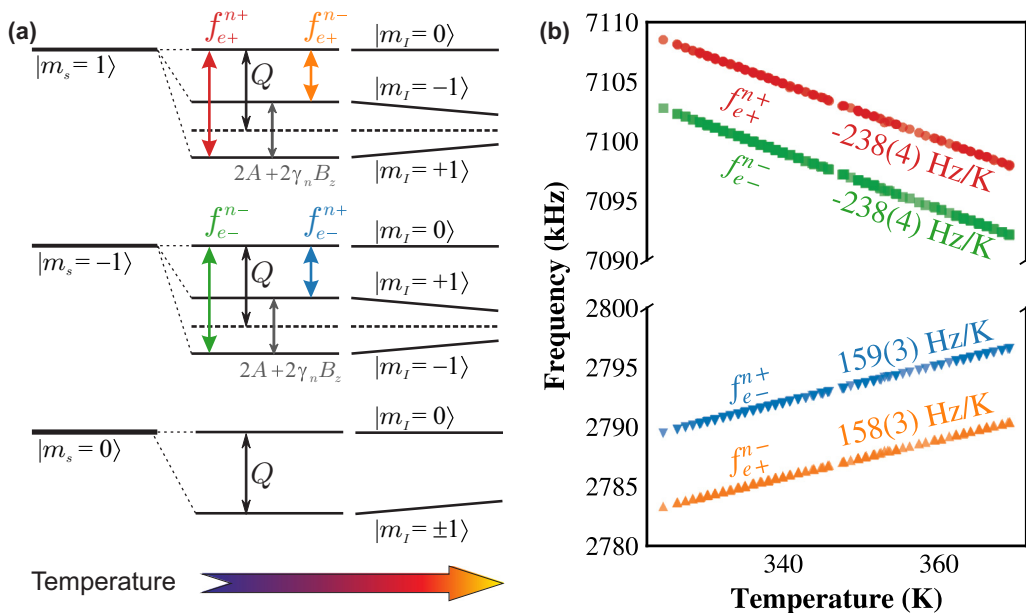
FIG. 3. (a) Schematic representation of the level structure shift due to temperature. (b) Shift of the NV hyperfine transition lines, with the color coding matching that in (a).
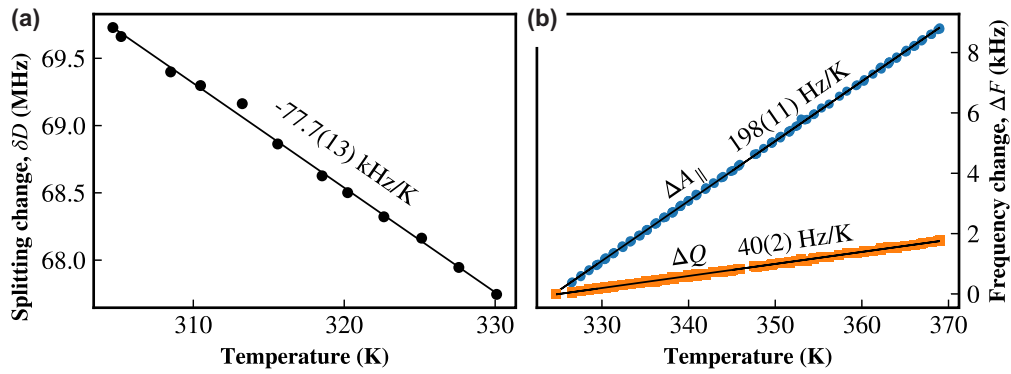
FIG. 4. (a) Dependence of electronic change in zero-field splitting (ZFS) on the temperature (with respect to 2800 MHz). (b) Dependence of the Q, $A_\parallel$ change on the temperature of the diamond. Clearly, a linear dependence is observed. Changes are depicted with respect to the -4946.0-kHz and -2159.6-kHz rfs.

To vary the temperature, a Peltier element is used with PI feedback from a digital thermometer (DS18B20) installed in the proximity of the diamond. The temperature is gradually changed in the range from 305 to 350 K. To exclude temperature measurement biasing due to the thermal junction between the diamond and thermometer, optical power dissipation and rf heating, we use the same ensemble of NV centers as that of the temperature sensor using the positions of ODMR lines from the MW scan. It is well known that zero-field splitting of the electron spin D changes with temperature [20,21], providing a means to implement a NV-based thermometer. However, because the temperature dependence of D varies between diamond samples, we also calibrate D against temperature for the sample used in the experiment [see Fig. 4(a) and Appendix F for more details].

Figure 3(b) presents the temperature dependence of the nuclear resonance position, determined as discussed above. With the help of Eqs. (3) and (4), the values of $Q(T)$ and $A_\parallel(T)$ are extracted for each temperature, as shown in Fig. 4(b). The relative temperature shift can be found by a linear fit of each curve, thus allowing us to find $\frac{dQ}{dT} = 40(2)$ Hz/K and $\frac{dA_\parallel}{dT} = 198(11)$ Hz/K. For error analysis, see Appendix E. We note that one can also deduce the temperature calibration independent values in our range of temperatures, $\frac{dA_\parallel}{dD} = -2.555(7) \times 10^{-3}$ and $\frac{dQ}{dD} = -5.03(5) \times 10^{-4}$, which relate the shift of the electron and nuclear spin with the temperature.

The hyperfine term $A_\parallel$ can be expressed as follows [29]:

$$A_\parallel = f_A + 2a_{A_1},$$

where f_A is the Fermi contact term and a_A is a dipole-dipole nuclear-electron interaction, which were estimated as $-h \cdot 2.5$ MHz and $h \cdot 187$ kHz, respectively [29], with h standing for the Plank constant. Thus, f_A is the dominant term in hyperfine coupling. The expression for f_A is

$$f_A = \gamma_{el}\gamma_n \frac{\mu_0}{4\pi\hbar^2}\left|\psi_{@n}^{el}\right|^2,$$

where γ_{el} and γ_n are the nuclear and electron gyromagnetic ratios, respectively, and $|\psi_{@n}^{el}| = \langle e|\delta(r - r_N)|e\rangle$ is the electron-spin density at the ^{14}N nuclear site. We note that it was speculated that the dependence of spin density on distance is exponential [30,31] Hence, the dependence of $A_\parallel$ on temperature is as follows:

$$\frac{dA_\parallel}{dT} = \frac{dA_\parallel}{dr}\frac{dR}{dT} = \frac{A_\parallel}{r_0}\frac{dR}{dT},$$

where R is the distance between nitrogen and the nearest carbon atom and is equal to 0.252 nm, r_0 is the decay constant of the electron spin density, and dR/dT is equal to $-2.52(2) \times 10^{-5}$K^{-1} [20]. Taking r_0 as 0.3 nm (characteristic length of the diamond lattice), we obtained $\frac{dA_\parallel}{dT} \simeq -211$ Hz/K, which is within 10% of our experimental result. The remaining discrepancy could be due to the dipole-dipole interaction and thus requires further investigation.

We note that the quadrupole shift is an order of magnitude lower than the hyperfine interaction term. The quadrupole shift is likely due to the change in the electric-field gradient seen by the nuclear spin with expansion of the sample [32]. However, to our knowledge, the fraction of p orbitals into the nuclear spin site is low [32], which might be the reason for the low sensitivity to temperature.

The temperature-dependent shift in the ^{14}N nuclear spin associated with the hyperfine splitting of the NV center was experimentally measured. The shift of approximately 200 Hz/K turns out to be quite noticeable and must be taken into account in sensors utilizing nuclear spin, such as gyroscopes or magnetic field sensors. The major part of the shift comes from the hyperfine constant contribution $\frac{dA_\parallel}{dT} = 198(11)$ Hz/K and is well described by the Fermi contact term drift, while the quadrupole moment contribution $\frac{\partial Q}{\partial T} = 40(2)$ Hz/K is an order of magnitude less sensitive to temperature.

APPENDIX A: EXPERIMENTAL DETAILS

1. Experiment with permanent magnet

Our experimental setup allows for controlling a spin ensemble in bulk diamond at room temperature [see Fig. 1(a)]. For a light source, we used a 520-nm laser light with 100 mW of power, generated by a WSLD-520-001-K laser diode from Wave Spectrum. The laser diode was driven by a diode home-built driver, which stabilizes the output power when the laser is on and allows 100% on-off modulation of the output power with a <5-μs rise/fall time. Laser light was focused onto spots with widths on the $1/e$ level of $6 \times 11 \mu m$. As the sample for our research, we used a diamond plate polished perpendicular to the 111 crystallographic axis (Velman LLC) with approximately 14 ppm of NV centers. The fluorescence of the NV centers was collected with a parabolic concentrator (Edmund Optics). A constant magnetic field was formed by a permanent magnet on a rotation-translation mount. Alignment of the field was checked by matching three residual orientation frequencies. To exclude the effects of the temperature dependence of the magnetic field due to permanent magnet heat-up, an additional experiment with Helmholtz coils was performed (see below).

The MW field was formed by an antenna composed of two, 4 mm-diameter coaxial loops made out of 1-mm copper wire and separated by 4 mm with a diamond sample in between. These loops were terminated with parallel copper plates that formed a capacitor. This assembly forms an LC resonator, the resonance frequency of which can be tuned to the desired frequency of the NV-center ODMR transition. In our experiments, the resonator was excited by a weakly inductively coupled feed loop. A Stanford Research signal generator SG384 was the source of the MW signal and was quadrature modulated by a dual-channel direct digital synthesizer (DDS) signal and then amplified using a Minicircuits ZHL-16W-43X+ amplifier. The dual-channel DDS was implemented by a 100 megasample per second dual digital-to-analog converter, driven by a field-programmable gate array (FPGA). The antenna was fed through the circulator to avoid back reflections. The same construction, i.e., a single-channel 100 megasample per second DDS, was the source for the rf signal. The signal was amplified with a 30-W VectaWave VBA100-30 amplifier. The amplifier was directly connected to the antenna, which was formed by 2×10 loops of 0.2-mm copper wire. The MW Rabi frequency was set such that the pi pulse has a length of 700 ns with a 20-dBm output power. The rf amplifier power was adjusted to set the π pulse length at both frequencies.

Thermal contact from the Peltier element to the diamond sample was provided by a sapphire cylinder to avoid DC magnetic field disturbance and interference with microwave and radio-frequency fields.

2. Experiment with Helmholtz coils

To exclude the effect of the temperature influence on the magnetic field source, we carried out an additional experiment with Helmholtz coils and provided the final data in Fig. 5, showing that a change in the magnetic source type does not
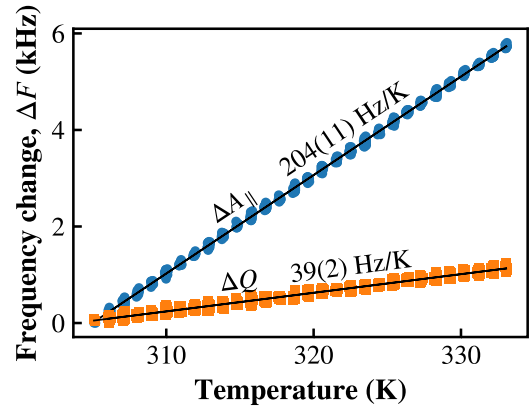
FIG. 5. Temperature dependence of the hyperfine constants obtained with Helmholtz coils used as the source of the magnetic field.

influence the experimental results. In this experiment, we found that $\frac{dA_\parallel}{dT} = 204(11)$ Hz/K and $\frac{dQ}{dD} = 39(2)$ Hz/K.

APPENDIX B: RABI OSCILLATIONS FOR NUCLEAR TRANSITIONS

To adjust the radio-frequency pulse times, we measured the nuclear Rabi oscillations on the $m_s = -1$ manifold by using the experimental sequence in Fig. 1(c) of the main text for a single data point. We fixed the rf to either f_{e-}^{n+} or f_{e-}^{n-} and the MW frequency to the $|m_s = 0, m_i = 0\rangle \leftrightarrow |m_s = -1, m_i = 0\rangle$ transition. The rf pulse time was varied from 0 to 2 ms, resulting in a Rabi oscillation signal. To remove the offset due to electronic spin decay, the Rabi experiment was repeated with the rf pulse disabled. The resulting data were subtracted from the Rabi oscillation signal, providing us with the data depicted in Fig. 6. The radio-frequency field amplitude for both nuclear transitions was adjusted to have a Rabi frequency close to 1.9 kHz, corresponding to a π-pulse duration of 263 μs.
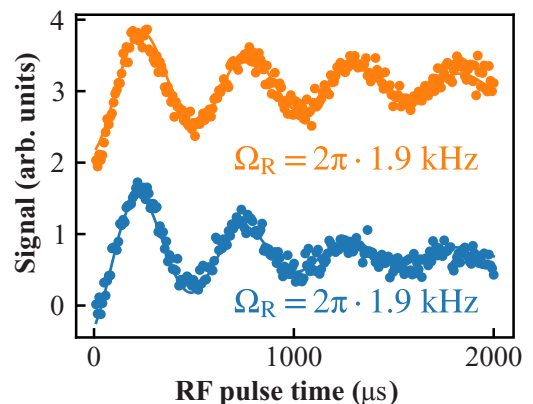
FIG. 6. Adjusted nuclear Rabi oscillations. The blue line corresponds to $f_{e-}^{n+} = 2.79$ MHz, and the yellow line corresponds to $f_{e-}^{n-} = 7.11$ MHz (the offset of 0.0002 was added for clarity).
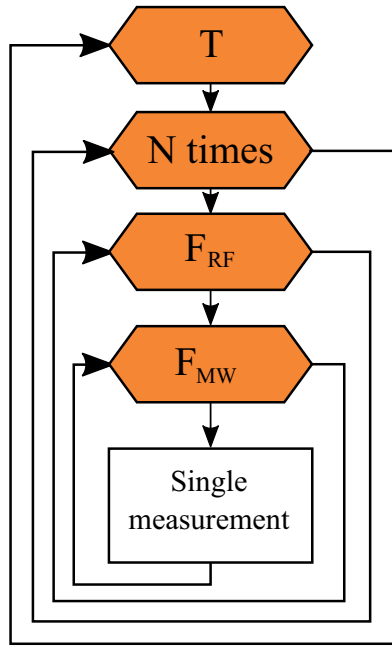
FIG. 7. Loop diagram of the experiment.

APPENDIX C: CYCLOGRAM OF THE MEASUREMENTS

To scan the temperature shifts of hyperfine constants, the algorithm described in Fig. 7 was utilized. There are four nested loops (see Fig. 7). The outermost loop (labeled "T," Fig. 7) represents the temperature sweep. The repeat loop (labeled "N times," Fig. 7) is nested inside the temperature sweep to repeat the resonance scan at a certain temperature. Typically, the number of repetitions is ten. To implement the resonance scan (as shown in Fig. 2), we scan the MW frequency (loop labeled "F_{MW}," Fig. 7) for each rf (loop labeled "F_{rf}", Fig. 7) and run the measurement (labeled "single measurement," Fig. 7) according to the sequence depicted in Fig. 1(c).

APPENDIX D: FITTING PROCEDURE FOR THE RESULTS OF A SINGLE MW/RF SCAN

The ODMR signal depicted in Figure 2 contains three resonances, corresponding to three hyperfine components. The amplitude of each resonance is linearly linked to the corresponding nuclear sublevel population. The shape was fitted with a function $L(f)$:

$$L(f) = \sum_{i=1}^{3} A_i \frac{\Delta_f{}^2}{(f - f_i)^2 + \Delta_f{}^2}, \qquad (D1)$$

where A_i, f_i, and Δ_f are fitting parameters (the amplitude, central frequency, and half width, respectively). The amplitude coefficient A_i thus provides information on nuclear populations, and f_i, on the electronic transition, corresponding to a specific nuclear state frequency. For ODMR slices with near-resonant nuclear rf π pulses, the independent fitting procedure is not stable due to the small amplitudes of some of the peaks. Therefore, the procedure described in the main text was implemented. The electronic resonant frequency was

recovered by averaging the stable fitting parameters of ODMR lines far from the rf resonance, 100 points at the beginning and end of the rf range [marked in blue in Fig. 2(a)].

APPENDIX E: ERROR ESTIMATION

We split all error sources into four groups, as discussed below.

1. Error estimation from fitting the *A* vs *D* and *Q* vs *D*

The error of the fitted data is taken from the fit estimated covariance matrix, obtained from the function curve_fit of the SCIPY.OPTIMIZE package (Virtanen *et al.,* 2020) with source data errors from the fit residuals.

The uncertainty of the electron resonance frequency for a single point has a mean error across all datasets of $\delta F_{\pm 1} \approx 0.8$ kHz, leading to an error of D estimation $\delta D = \frac{\delta F_{+1} + \delta F_{-1}}{2} = \delta F_{\pm 1}$. However, because a single measurement is long lasting, the temperature change will induce an additional error of approximately $\delta D_m^T = 8$ kHz , which was estimated as the difference in the D value between the start and end of a single measurement. We assume the latter to be the dominant source of error in the D estimation, thus leading to $\delta D = 8$ kHz. Because the least-squares fitting procedure uses the error of the dependent data, we transform δD into $\delta A_\parallel = \delta D \frac{dA_\parallel}{dD} \approx 20$ Hz and $\delta Q = \delta D \frac{dQ}{dD} \approx 4$ Hz. The values for $\frac{dA_\parallel}{dD}$ and $\frac{dQ}{dD}$ are taken from the fit.

The uncertainty for nuclear resonance frequencies $f_{e\pm}^{n\pm}$ is on the order of $\delta f_{e\pm}^{n\pm} = 100$ Hz (ranging from 63 to 300 Hz) for all datasets, dominating the error induced by the δD uncertainty. According to formulas (3) and (4), the random error for dependent variables is $\delta A_\parallel = \delta Q = \delta f_{e\pm}^{n\pm}$.

We note that the fit residuals for $\frac{dA_\parallel}{dD}$ and $\frac{dQ}{dD}$ give estimation errors for $A_\parallel$ and Q of approximately 50 Hz (ranging from 30 to 80 Hz), being less than a lesser error of the fit to a complex shape of the rf resonance that cannot be fitted well with a single Lorentzian.

2. Error estimation from grouping the data into series

For statistical error estimation, we randomly split each set of data $\{D^{(i)}, A_\parallel^{(i)}, Q^{(i)}\}$ into four equal groups $\{\{i_k\}\}$ and fit the data in each group to obtain

$$\alpha_k = \frac{dA_\parallel}{dD}\Big|_{\{D^{(i_k)}, A_\parallel^{(i_k)}\}}$$
$$\beta_k = \frac{dQ}{dD}\Big|_{\{D^{(i_k)}, Q^{(i_k)}\}}. \qquad (E1)$$

As the final values, we use $\alpha = \overline{\alpha_k}$, $\beta = \overline{\beta_k}$, with errors $\delta\alpha = \sqrt{\frac{\sum_k (\alpha_k - \overline{\alpha_k})^2}{3}}$ and $\delta\beta = \sqrt{\frac{\sum_k (\beta_k - \overline{\beta_k})^2}{3}}$.

We use this estimation for four spots of the same diamond plate:

Spot	Group, k	α	β
1	1	$-2.544(4)\times10^{-3}$	$-5.04(3)\times10^{-4}$
	2	$-2.548(5)\times10^{-3}$	$-5.00(3)\times10^{-4}$
	3	$-2.548(5)\times10^{-3}$	$-5.03(3)\times10^{-4}$
	4	$-2.545(4)\times10^{-3}$	$-5.01(3)\times10^{-4}$
	All	$-2.546(2)\times10^{-3}$	$-5.02(1)\times10^{-4}$
	All fitted	$-2.546(2)\times10^{-3}$	$-5.02(1)\times10^{-4}$
2	1	$-2.554(5)\times10^{-3}$	$-4.99(5)\times10^{-4}$
	2	$-2.558(7)\times10^{-3}$	$-5.07(6)\times10^{-4}$
	3	$-2.572(6)\times10^{-3}$	$-5.01(6)\times10^{-4}$
	4	$-2.574(7)\times10^{-3}$	$-5.02(6)\times10^{-4}$
	All	$-2.564(9)\times10^{-3}$	$-5.02(3)\times10^{-4}$
	All fitted	$-2.565(3)\times10^{-3}$	$-5.02(3)\times10^{-4}$
5	1	$-2.550(4)\times10^{-3}$	$-5.10(3)\times10^{-4}$
	2	$-2.551(3)\times10^{-3}$	$-5.09(2)\times10^{-4}$
	3	$-2.554(3)\times10^{-3}$	$-5.10(2)\times10^{-4}$
	4	$-2.555(3)\times10^{-3}$	$-5.13(3)\times10^{-4}$
	All	$-2.553(2)\times10^{-3}$	$-5.11(1)\times10^{-4}$
	All fitted	$-2.553(2)\times10^{-3}$	$-5.11(2)\times10^{-4}$
4	1	$-2.556(6)\times10^{-3}$	$-4.97(5)\times10^{-4}$
	2	$-2.560(6)\times10^{-3}$	$-4.99(4)\times10^{-4}$
	3	$-2.556(6)\times10^{-3}$	$-4.92(5)\times10^{-4}$
	4	$-2.548(5)\times10^{-3}$	$-4.98(5)\times10^{-4}$
	All	$-2.555(4)\times10^{-3}$	$-4.97(3)\times10^{-4}$
	All fitted	$-2.555(3)\times10^{-3}$	$-4.97(2)\times10^{-4}$
	Average	$-2.555(7)\times10^{-3}$	$-5.03(5)\times10^{-4}$

where "All" refers to the values obtained from averaging by group and "All fitted" means the fit for all data, not just the data of one group.

We note that the error of each group value (estimated as a covariance from the least square fit for the group data) is approximately the same as the statistical standard deviation for all groups. The error in the value obtained from the fit over all data groups is approximately $\sqrt{N_{\text{group}}} = 2$ lower than the error of each subgroup, which is in compliance with the standard error of the mean scaling.

After fitting all the data, we averaged the obtained values and set the standard deviations of the values as the errors of determination for the final α and β values.

3. Perturbation theory corrections

Consider the full Hamiltonian for the NV center:

$$
\begin{aligned}
H = {} & DS_z^2 + \gamma_e \boldsymbol{BS} + QI_z^2 + \gamma_n \boldsymbol{BI} \\
& + A_\parallel S_z I_z + A_\perp (S_x I_x + I_x S_x) \,.
\end{aligned} \tag{E2}
$$

We split the Hamiltonian into diagonal term $H^{(0)}$ and non-diagonal part V according to the formulas

$$
H^{(0)} = DS_z^2 + \gamma_e B_z S_z + \gamma_n B_z I_z + A_\parallel S_z I_z, \tag{E3}
$$

$$
V = \gamma_e B_x S_x + \gamma_n B_x I_x + A_\perp (S_x I_x + I_x S_x). \tag{E4}
$$

According to second-order perturbation theory, second-order corrections to the eigenvalues of $H^{(0)}$ are calculated:

$$
\delta E_{m_s, m_i} = \sum_{i \neq m_s, j \neq m_i} \frac{|i, j|V|m_s, m_i|^2}{E_{m_s, m_i}^{(0)} - E_{i, j}^{(0)}}. \tag{E5}
$$

For the transition frequencies mentioned in the article, the following corrections are made:

From the equations obtained by using Eqs. (3) and (4) of the main text, we obtain the corrections for the Q, $A_\parallel$ estimations:

$$
\begin{aligned}
\delta Q^* = {} & -\frac{A_\perp^2 (D - Q)}{(D - Q)^2 - (B_z \gamma_e - B_z \gamma_n)^2} \\
& + \frac{1}{2} \frac{A_\perp^2 (-A_\parallel + D + Q)}{-(B_z \gamma_e - B_z \gamma_n)^2 + (-A_\parallel + D + Q)^2} \\
& - \frac{1}{2} \frac{B_x^2 D \gamma_e^2}{-B_z^2 \gamma_e^2 + D^2} + \frac{3}{4} \frac{B_x^2 Q \gamma_n^2}{Q^2 - (A_\parallel + B_z \gamma_n)^2} \\
& + \frac{3}{4} \frac{B_x^2 Q \gamma_n^2}{Q^2 - (A_\parallel - B_z \gamma_n)^2} \\
& + \frac{1}{4} \frac{B_x^2 \gamma_e^2 (-A_\parallel + D)}{-B_z^2 \gamma_e^2 + (-A_\parallel + D)^2} \\
& + \frac{1}{4} \frac{B_x^2 \gamma_e^2 (A_\parallel + D)}{-B_z^2 \gamma_e^2 + (A_\parallel + D)^2},
\end{aligned} \tag{E6}
$$

Frequency	Frequency correction term	Value
f_{e-}^{n-}	$\delta E_{-1,0} - \delta E_{-1,-1}$	$\dfrac{A_\perp^2}{-B_z\gamma_e + B_z\gamma_n + D - Q} - \dfrac{B_x^2 Q\,\gamma_n^2}{Q^2 - (-A_\parallel + B_z\gamma_n)^2} - \dfrac{1}{2}\dfrac{B_x^2\gamma_e^2}{A_\parallel - B_z\gamma_e + D} + \dfrac{1}{2}\dfrac{B_x^2\gamma_e^2}{-B_z\gamma_e + D} + \dfrac{1}{2}\dfrac{B_x^2\gamma_n^2}{-A_\parallel + B_z\gamma_n - Q}$
f_{e-}^{n+}	$\delta E_{-1,0} - \delta E_{-1,+1}$	$-\dfrac{A_\perp^2}{-A_\parallel - B_z\gamma_e + B_z\gamma_n + D + Q} + \dfrac{A_\perp^2}{-B_z\gamma_e + B_z\gamma_n + D - Q} - \dfrac{1}{2}\dfrac{B_x^2\gamma_e^2}{-A_\parallel - B_z\gamma_e + D} + \dfrac{1}{2}\dfrac{B_x^2\gamma_e^2}{-B_z\gamma_e + D} + \dfrac{B_x^2\gamma_n^2}{A_\parallel - B_z\gamma_n - Q} + \dfrac{1}{2}\dfrac{B_x^2\gamma_n^2}{-A_\parallel + B_z\gamma_n - Q}$
f_{e+}^{n-}	$\delta E_{+1,0} - \delta E_{+1,-1}$	$-\dfrac{A_\perp^2}{-A_\parallel + B_z\gamma_e - B_z\gamma_n + D + Q} + \dfrac{A_\perp^2}{B_z\gamma_e - B_z\gamma_n + D - Q} - \dfrac{1}{2}\dfrac{B_x^2\gamma_e^2}{-A_\parallel + B_z\gamma_e + D} + \dfrac{1}{2}\dfrac{B_x^2\gamma_e^2}{B_z\gamma_e + D} + \dfrac{B_x^2\gamma_n^2}{A_\parallel + B_z\gamma_n - Q} + \dfrac{1}{2}\dfrac{B_x^2\gamma_n^2}{-A_\parallel - B_z\gamma_n - Q}$
f_{e+}^{n+}	$\delta E_{+1,0} - \delta E_{+1,+1}$	$\dfrac{A_\perp^2}{B_z\gamma_e - B_z\gamma_n + D - Q} - \dfrac{B_x^2 Q\,\gamma_n^2}{Q^2 - (-A_\parallel - B_z\gamma_n)^2} - \dfrac{1}{2}\dfrac{B_x^2\gamma_e^2}{A_\parallel + B_z\gamma_e + D} + \dfrac{1}{2}\dfrac{B_x^2\gamma_e^2}{B_z\gamma_e + D} + \dfrac{1}{2}\dfrac{B_x^2\gamma_n^2}{-A_\parallel - B_z\gamma_n - Q}$

$$\delta A_\parallel^* - \frac{0.25\, A_\perp^2(-2.0\, A_\parallel + 2.0\, D + 2.0\, Q)}{-(B_z\gamma_e - B_z\gamma_n)^2 + (-A_\parallel + D + Q)^2}$$

$$-\frac{0.125\, B_x^2\gamma_e^2(-2.0\, A_\parallel + 2.0\, D)}{-B_z^2\gamma_e^2 + (-A_\parallel + D)^2}$$

$$+\frac{0.125\, B_x^2\gamma_e^2(2.0\, A_\parallel + 2.0\, D)}{-B_z^2\gamma_e^2 + (A_\parallel + D)^2}$$

$$-\frac{0.125\, B_x^2\gamma_n^2(-2.0\, A_\parallel + 2.0\, Q)}{-B_z^2\gamma_n^2 + (A_\parallel - Q)^2}$$

$$+\frac{0.125\, B_x^2\gamma_n^2(2.0\, A_\parallel + 2.0\, Q)}{-B_z^2\gamma_n^2 + (-A_\parallel - Q)^2}, \tag{E7}$$

$$\delta Q^* = -1.73 \times 10^{-10} A_\perp^2 - 0.0344 B_x^2, \tag{E8}$$

$$\delta A_\parallel^* = -1.74 \times 10^{-10} A_\perp^2 - 1.03 B_x^2. \tag{E9}$$

According to the data fit of the optically detected magnetic resonance (Fig. 8) transverse to the 111 orientation magnetic field $B_x = 1.3$ G, the errors of the temperature dependences
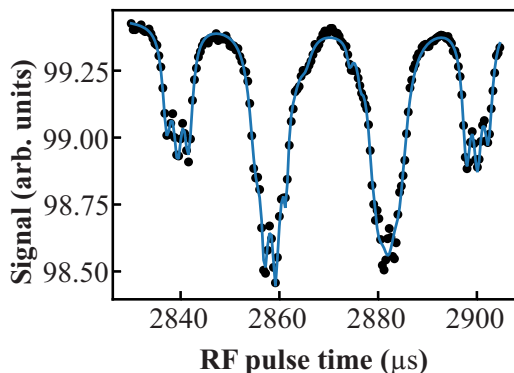
FIG. 8. Optically detected magnetic resonance for B_x estimation.

$\alpha' = \frac{dA_\parallel}{dT}$ and $\beta' = \frac{dQ}{dT}$ due to the temperature dependence of $\frac{dA_\perp}{dT}$, $\frac{dB_x}{dT}$ is

$$\left|\delta_{\alpha'}^{(V)}\right| < \left| 1.73 \times 10^{-10} \times 2A_\perp \frac{dA_\perp}{dT}\right| + \left| 0.034 \times 2\, B_x \frac{dB_x}{dT}\right|, \tag{E10}$$

$$\left|\delta_{\beta'}^{(V)}\right| < \left| 1.74 \times 10^{-10} \times 2A_\perp \frac{dA_\perp}{dT}\right| + \left| 1.03 \times 2\, B_x \frac{dB_x}{dT}\right|. \tag{E11}$$

During the experiment, B_z—the magnetic field change—was within $\Delta B_z = 0.05$ G in the temperature range of $\Delta T = 60$ K. From the ODMR fit, the transverse B_x field was estimated to be 1.3 G (Fig. 8). Supposing that the relative change in B_x and B_z is the same, the maximum estimation for $|\frac{dB_x}{dT}| = \frac{B_x}{B_z}\frac{\Delta B_z}{\Delta T} = \frac{1.3}{11}\frac{0.05}{60} = 10^{-4}\frac{\text{G}}{\text{K}}$. Supposing that $\frac{dA_\perp}{dT}$ is of the same order as $\frac{dA_\parallel}{dT} = -200\frac{\text{Hz}}{\text{K}}$ and using $A_\perp = -2.7$ MHz finally lead to the following error:

$$\left|\delta_\alpha^{(V)}\right| \approx \left|\delta_\beta^{(V)}\right| \approx 0.2\frac{\text{Hz}}{\text{K}}. \tag{E12}$$

Here, the $\frac{dA_\perp}{dT}$-induced term is at least 3 orders of magnitude higher than the B_x-induced term. Thus, the transverse field could vary in a broader range with a negligible impact on the error, and its absolute value of 1.3 G is not a precision-limiting factor.

4. Errors of temperature calibration

The error of the temperature calibration $D(T)$ includes the following errors: temperature sensor error δT_{sensor}, temperature offset error δT_{offset}, and fitting random error. $\delta T_{\text{sensor}} = 0.5$ K for the DS18B20 temperature sensor utilized in the experiment. The uncertainty due to the sensor for $\kappa = \frac{dD}{dT}$ is

$$\delta\kappa_{\text{sensor}} = |\kappa|\frac{\delta T_{\text{sensor}}}{T_{\text{max}} - T_{\text{min}}} = 77.7\frac{0.5}{330 - 305} = 1.6\frac{\text{kHz}}{\text{K}}. \tag{E13}$$
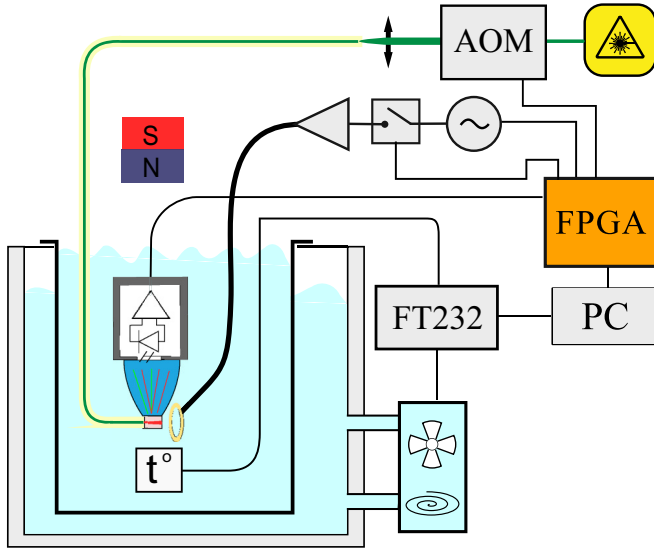
FIG. 9. Setup for electron-spin ZFS calibration.

To estimate the temperature offset error, we note that in the case of thermal equilibrium, the offset between the environmental temperature and the heated spot temperature with a constant heat source and the same thermal constant relative to the environment will be constant. Thus, although the absolute temperature might change with the optical power delivered to the sample, the derivative of the temperature of the environment will be the same. To further prove this, we record the temperature as a function of the laser power and observe minor changes in the temperature on the order of $\delta T_{\text{offset}} = 1.2°$ per 100 mW of laser power, which we consider as a systematic error in our measurement. To account for this, we consider the calibration of κ to be with systematic uncertainty

$$\delta\kappa_{\text{offset}} = |\kappa|\frac{\delta T_{\text{offset}}}{T_{\text{max}} - T_{\text{min}}} = 77.7\frac{1.2}{330 - 305} = 3.7\frac{\text{kHz}}{\text{K}}.$$
(E14)

$\delta\kappa_{\text{random}} = 1.3\frac{\text{kHz}}{\text{K}}$ is obtained from the fitting procedure.

The final uncertainty for κ is

$$\delta\kappa = \sqrt{\delta\kappa_{\text{sensor}}^2 + \delta\kappa_{\text{offset}}^2 + \delta\kappa_{\text{random}}^2} = 4.2\frac{\text{kHz}}{\text{K}}.$$
(E15)

5. Error estimation for temperature dependence

For the final temperature coefficients of $\alpha' = \frac{dA_\parallel}{dT} = \frac{dA_\parallel}{dD}\frac{dD}{dT}$ and $\beta' = \frac{dQ}{dT} = \frac{dQ}{dD}\frac{dD}{dT}$, we estimate the relative uncertainty:

$$U'_{\alpha'} = \sqrt{\left(\frac{\delta_{\alpha'}^{(V)}}{\alpha'}\right)^2 + \left(\frac{\delta_{\alpha}^{(random)}}{\alpha}\right)^2 + \left(\frac{\delta\kappa}{\kappa}\right)^2},$$
(E16)

$$U'_{\beta'} = \sqrt{\left(\frac{\delta_{\beta'}^{(V)}}{\beta'}\right)^2 + \left(\frac{\delta_{\beta}^{(random)}}{\beta}\right)^2 + \left(\frac{\delta\kappa}{\kappa}\right)^2}.$$
(E17)

The final relative uncertainty is $U'_{\alpha'} = 5.5\%$, $U'_{\beta'} = 5.6\%$. The final values are $\frac{dA_\parallel}{dT} = 200(10)\ \frac{\text{Hz}}{\text{K}}$ and $\frac{dQ}{dT} = 39(2)\ \frac{\text{Hz}}{\text{K}}$.

APPENDIX F: CALIBRATION OF ZERO-FIELD SPLITTING AGAINST TEMPERATURE

A water-filled thermostat (Ultra-Thermostat Type U 10) was used with diamond, a microwave antenna and a photodiode submerged in water (Fig. 9). For optical pumping, we used a 532-nm laser (Laser Quantum Finesse Pure 12 W) with 100 mW of power coupled to a single-mode optical fiber. The free end of the fiber was attached to the diamond. The temperature of the water inside the thermostat was controlled with a PI controller and sampled by a digital thermometer (DS18B20) placed in the proximity of the diamond. Fluorescence collection was performed with a compound parabolic concentrator with a considerably reduced collection efficiency in water due to the higher refractive index. Because no optical low-pass filter was utilized, the fluorescence contrast was greatly reduced; however, the signal-to-noise ratio was decent. The photodetector used was PDB-C609-2, placed with a transimpedance amplifier on an inch-diameter PCB. To protect electronics and photodiodes from water damage, the
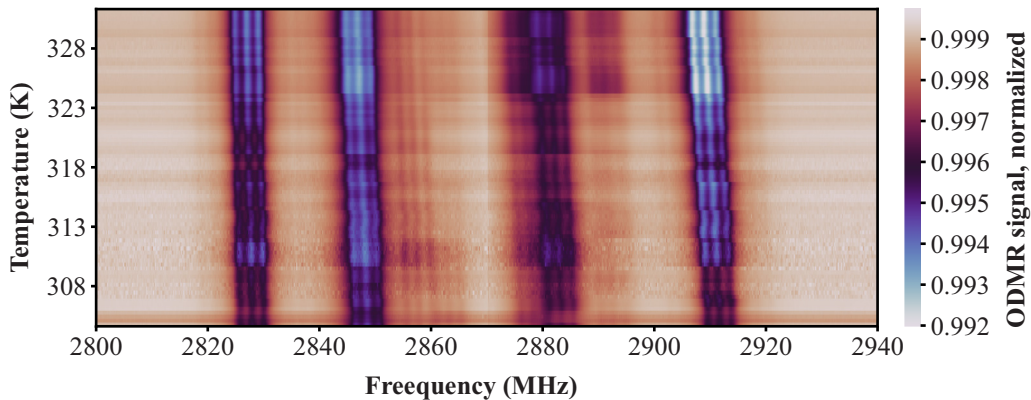
FIG. 10. Pulsed ODMR scans with sweeping of the temperature.

photodetector was sealed with UV adhesive. A bias magnetic field was applied with a permanent magnet. A small copper coil attached to a coaxial wire was utilized as a microwave antenna.

The temperature was swept from 305 to 336 K with a 2.5 K step, with pauses of 20 min to wait for thermalization at each temperature point and running of the pulsed ODMR measurement for 15 min with simultaneous control of the temperature. As a result, a set of ODMR data was obtained (Fig. 10). To define D, the data were fitted with four pairs of triplet resonance lines [see Eq. (D1)]. From the leftmost and rightmost resonance positions f_{-1}, f_{+1}, zero-field

splitting was calculated as

$$D = \frac{f_{-1} + f_{+1}}{2}, \tag{F1}$$

resulting in Fig. 4(a). Because the permanent magnet was in close proximity to the thermostat, the magnetic field was reduced from 14.9 to 14.5 G while being heated up and was defined from the NV-center Zeeman splitting between $m_s = \pm 1$ levels by using the formula $B = \frac{f_{+1} - f_{-1}}{2\gamma_e}$, where $\gamma_e = 28$ GHz/T stands for the electron-spin gyromagnetic ratio.

[1] A. O. Sushkov, N. Chisholm, I. Lovchinsky, M. Kubo, P. K. Lo, S. D. Bennett, D. Hunger, A. Akimov, R. L. Walsworth, H. Park, and M. D. Lukin, Nano Lett. **14**, 6443 (2014).

[2] T. Wolf, P. Neumann, K. Nakamura, H. Sumiya, T. Ohshima, J. Isoya, and J. Wrachtrup, Phys. Rev. X **5**, 041001 (2015).

[3] J. Scheuer, I. Schwartz, S. Müller, Q. Chen, I. Dhand, M. B. Plenio, B. Naydenov, and F. Jelezko, Phys. Rev. B **96**, 174436 (2017).

[4] M. Chipaux, A. Tallaire, J. Achard, S. Pezzagna, J. Meijer, V. Jacques, J.-F. Roch, and T. Debuisschert, Eur. Phys. J. D **69**, 166 (2015).

[5] A. Ajoy, U. Bissbort, M. D. Lukin, R. L. Walsworth, and P. Cappellaro, Phys. Rev. X **5**, 011001 (2015).

[6] A. Nagl, S. R. Hemelaar, and R. Schirhagl, Anal. Bioanal. Chem. **407**, 7521 (2015).

[7] P. C. Maurer, G. Kucsko, C. Latta, L. Jiang, N. Y. Yao, S. D. Bennett, F. Pastawski, D. Hunger, N. Chisholm, M. Markham, D. J. Twitchen, J. I. Cirac, and M. D. Lukin, Science **336**, 1283 (2012).

[8] P. Neumann, J. Beck, M. Steiner, F. Rempp, H. Fedder, P. R. Hemmer, J. Wrachtrup, and F. Jelezko, Science **329**, 542 (2010).

[9] T. Chakraborty, J. Zhang, and D. Suter, New J. Phys. **19**, 073030 (2017).

[10] S. Zaiser, T. Rendler, I. Jakobi, T. Wolf, S.-Y. Lee, S. Wagner, V. Bergholm, T. Schulte-Herbrüggen, P. Neumann, and J. Wrachtrup, Nat. Commun. **7**, 12279 (2016).

[11] M. P. Ledbetter, K. Jensen, R. Fischer, A. Jarmola, and D. Budker, Phys. Rev. A **86**, 052116 (2012).

[12] A. Ajoy and P. Cappellaro, Phys. Rev. A **86**, 062104 (2012).

[13] D. E. J. Waddington, M. Sarracanie, H. Zhang, N. Salameh, D. R. Glenn, E. Rej, T. Gaebel, T. Boele, R. L. Walsworth, D. J. Reilly, and M. S. Rosen, Nat. Commun. **8**, 15118 (2017).

[14] J. Scheuer, I. Schwartz, Q. Chen, D. Schulze-Sünninghausen, P. Carl, P. Höfer, A. Retzker, H. Sumiya, J. Isoya, B. Luy, M. B. Plenio, B. Naydenov, and F. Jelezko, New J. Phys. **18**, 013040 (2016).

[15] J. H. Shim, I. Niemeyer, J. Zhang, and D. Suter, Phys. Rev. A **87**, 012301 (2013).

[16] A. Dréau, P. Spinicelli, J. R. Maze, J.-F. Roch, and V. Jacques, Phys. Rev. Lett. **110**, 060502 (2013).

[17] D. Pagliero, A. Laraoui, J. D. Henshaw, and C. A. Meriles, Appl. Phys. Lett. **105**, 242402 (2014).

[18] H. Clevenson, M. E. Trusheim, T. Schroder, C. Teale, D. Braje, and D. Englund, Nat. Phys. **11**, 393 (2015).

[19] S. M. Blakley, I. V. Fedotov, S. Y. Kilin, and A. M. Zheltikov, Opt. Lett. **40**, 3727 (2015).

[20] V. M. Acosta, E. Bauch, M. P. Ledbetter, A. Waxman, L.-S. Bouchard, and D. Budker, Phys. Rev. Lett. **104**, 070801 (2010).

[21] I. V. Fedotov, N. A. Safronov, Y. G. Ermakova, M. E. Matlashov, D. A. Sidorov-Biryukov, A. B. Fedotov, V. V. Belousov, and A. M. Zheltikov, Sci. Rep. **5**, 15737 (2015).

[22] G. Kucsko, P. C. Maurer, N. Y. Yao, M. Kubo, H. J. Noh, P. K. Lo, H. Park, and M. D. Lukin, Nature (London) **500**, 54 (2013).

[23] D. M. Toyli, D. J. Christle, A. Alkauskas, B. B. Buckley, C. G. Van de Walle, and D. D. Awschalom, Phys. Rev. X **2**, 031001 (2012).

[24] X.-D. Chen, C.-H. Dong, F.-W. Sun, C.-L. Zou, J.-M. Cui, Z.-F. Han, and G.-C. Guo, Appl. Phys. Lett. **99**, 161903 (2011).

[25] E. H. Chen, H. A. Clevenson, K. A. Johnson, L. M. Pham, D. R. Englund, P. R. Hemmer, and D. A. Braje, Phys. Rev. A **95**, 053417 (2017).

[26] P. Kapitanova, V. V. Soshenko, V. V. Vorobyov, D. Dobrykh, S. V. Bolshedvorskii, V. N. Sorokin, and A. V. Akimov, JETP Lett. **108**, 588 (2018).

[27] V. V. Soshenko, O. R. Rubinas, V. V. Vorobyov, S. V. Bolshedvorskii, P. V. Kapitanova, V. N. Sorokin, and A. V. Akimov, Bull. Lebedev Phys. Inst. **45**, 237 (2018).

[28] B. Smeltzer, J. McIntyre, and L. Childress, Phys. Rev. A **80**, 050302(R) (2009).

[29] M. W. Doherty, F. Dolde, H. Fedder, F. Jelezko, J. Wrachtrup, N. B. Manson, and L. C. L. Hollenberg, Phys. Rev. B **85**, 205203 (2012).

[30] A. P. Nizovtsev, S. Y. Kilin, C. Tietz, F. Jelezko, and J. Wrachtrup, Phys. B: Condens. Matter **308-310**, 608 (2001).

[31] M. Łuszczek, R. Laskowski, and P. Horodecki, Phys. B: Condens. Matter **348**, 292 (2004).

[32] O. D. Tucker, M. E. Newton, and J. M. Baker, Phys. Rev. B **50**, 15586 (1994).